The Cape Canaveral Sea and River Breezes: Kinematic Structure and Convective Initiation

NEIL F. LAIRD AND DAVID A. R. KRISTOVICH

Illinois State Water Survey, Champaign, Illinois

ROBERT M. RAUBER

Department of Atmospheric Sciences, University of Illinois, Urbana, Illinois

HARRY T. OCHS III

Illinois State Water Survey, Champaign, Illinois

L. JAY MILLER

National Center for Atmospheric Research, Boulder, Colorado

(Manuscript received 12 September 1994, in final form 27 March 1995)

ABSTRACT

This study examines complex flow patterns associated with the Cape Canaveral sea breeze and sea-breeze front using dual-Doppler radar, sounding, and surface data collected on 26 July 1991 during the Convection and Precipitation/Electrification Experiment. This case focuses on (a) the structure of the sea breeze, an associated trailing convergence line, river-induced convergence zones, and thunderstorm outflow boundaries, and (b) the development of convection where these features interacted.

Variations in the direction of the sea breeze in the vicinity of irregular coastlines, such as Cape Canaveral, can lead to persistent zones of convergence within the sea-breeze air. The findings show that these zones of convergence, in turn, can locally increase the depth of the sea-breeze air and create circulations at the top of the sea breeze, which can support the development of convection. The observational study is the first to document the development and evolution of the trailing convergence line over Cape Canaveral and show that its presence can be instrumental in thunderstorm initiation.

Small inland water bodies, such as the Indian River, can have a strong influence on the location where thunderstorms first develop as the sea breeze propagates inland. Divergence over the small, relatively cooler Indian River during daytime was sufficient to maintain a quasi-stationary convergence zone that, when approached and disrupted by the sea-breeze front, triggered thunderstorms. The intersection point between the sea-breeze front and the river-induced convergence zone identified the location where successive thunderstorms developed during the day.

1. Introduction

Observations and both theoretical and numerical models have been used to examine numerous aspects of sea- and lake-breeze circulations. Much of the work has been devoted to understanding their roles in pollution dispersal, initiation of convection and climatic characteristics of large cities located on the shores of large bodies of water. Many studies (e.g., Byers and Rodebush 1948; Gentry and Moore 1954; Frank et al. 1967; Nicholls et al. 1991; Lyons et al. 1992) have shown that convective thunderstorms frequently form near and ahead of sea-breeze fronts. Indeed, sea-breeze circulations are thought to be the major factors determining where precipitation occurs over Florida (Pielke 1974).

Coastline shape, synoptic-scale winds, and water bodies close to the coastline influence sea-breeze frontal morphology. Several numerical studies (e.g., McPherson 1970; Abbs 1983; Arritt 1989; Cautenet and Rosset 1989; Zhong et al. 1991) have shown that the convergence patterns (i.e., vertical motion fields) associated with the sea breeze are altered along irregular coastlines. Pielke (1974) and Zhong and Takle (1993) numerically showed that the characteristics of the sea-breeze circulation over southern and east-central Flor-

Corresponding author address: Neil F. Laird, Illinois State Water Survey, Office of Cloud and Precipitation Research, 2204 Griffith Dr., Champaign, IL 61820-7495.
E-mail: laird@sundog.sws.uiuc.edu

© 1995 American Meteorological Society

ida, respectively, are also sensitive to synoptic-scale wind direction and speed. Thorough reviews of studies of sea breeze research can be found in Pielke (1984), Wakimoto and Atkins (1994), and the National Research Councils' review of coastal meteorology (1992).

Sea-breeze circulations have been examined recently in the Kennedy Space Center/Cape Canaveral (KSC/CC) area during both the Kennedy Space Center Atmospheric Boundary Layer Experiment (KABLE) (see Taylor et al. 1990) and the Convection and Precipitation/Electrification (CaPE) Experiment (Gray 1991). In a modeling effort associated with KABLE, Zhong et al. (1991) found that the presence of the Indian and Banana Rivers and the Mosquito Lagoon resulted in a convergence pattern that was quite different from that expected in a simple sea-breeze circulation. Weak subsidence over the rivers and lagoon, associated with the difference in surface heat flux between the rivers and adjacent land areas, disrupted the "normal" convergence pattern expected with a simple sea-breeze front. Atchison and Taylor (1992), Zhong and Takle (1993), and others, determined that this convergence pattern was quite sensitive to the direction and speed of synoptic-scale winds in that region. Watson et al. (1991) examined the area-averaged convergence field in this region and developed methods for prediction of cloud-to-ground lightning. These studies give important details about the resulting boundary layer convergence fields that may be expected in the Cape Canaveral region.

This paper documents the structure and evolution of the easterly sea-breeze inflow (hereafter called sea breeze) and the sea-breeze front in the vicinity of the irregular coastline near Cape Canaveral, the interaction of the sea-breeze front with quasi-stationary circulations associated with inland rivers, and the development of a trailing convergence line behind the sea-breeze front. We show that the trailing convergence line deepened the sea breeze in a local region and played a key role in the formation of a thunderstorm behind the sea-breeze front and above the sea breeze. The evolution of these features and the subsequent development of convection are documented using dual-Doppler radar, sounding, and surface data taken during the CaPE experiment on 26 July 1991.

2. Data sources and analysis methods

This study uses data collected during the CaPE experiment conducted in east-central Florida during the summer of 1991 (Gray 1991). The primary dataset used in this study was taken by the National Center for Atmospheric Research (NCAR) CP-3 and CP-4 5-cm-wavelength radars, which provided dual-Doppler coverage during CaPE. On 26 July both radars performed sector scans within the northern dual-Doppler lobe (Fig. 1). Surface measurements were provided by the NCAR Portable Automated Mesonet (PAM) II. Low-level data were taken by the Air Force/KSC WINDS tower network. Atmospheric sounding data from the Cape Canaveral Air Station (CCAS) and soundings during the takeoff and landing of the Wyoming King Air were used to examine the vertical structure of the atmosphere on either side of the sea-breeze front.

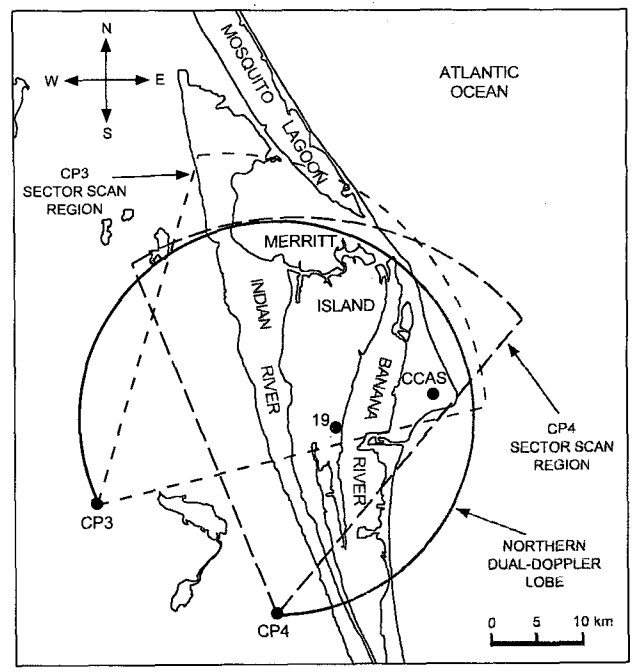

FIG. 1. Map showing Cape Canaveral and the northern CaPE study area. Positions of the NCAR radars (CP-3 and CP-4), the northern dual-Doppler lobe, and each radar's approximate sector scan region from 26 July are shown. The location of PAM II station 19 is labeled along with the Cape Canaveral Air Station (CCAS) sounding site.

Dual-Doppler analyses were performed using data taken from the CP-3 and CP-4 radars (Fig. 1). The radars were separated by a 23-km baseline. The radar equivalent reflectivity factor (hereafter called reflectivity) and radial velocity fields were interpolated to a Cartesian grid using the NCAR/Mesoscale and Microscale Meteorology Division (MMM) sorted position radar interpolation program (SPRINT) (Mohr and Vaughan 1979; Miller et al. 1986). The horizontal extent of the analysis region was 60 km × 50 km with a grid spacing of 400 m, while the vertical grid was spaced at 300 m. Dual-Doppler syntheses of the horizontal winds, calculation of derived fields and creation of graphical displays of the data were done with the NCAR/MMM custom editing and display of reduced information in Cartesian space program (CEDRIC) (Mohr et al. 1986). In addition, the NCAR/MMM planned position indicator (MMM PPI) program was

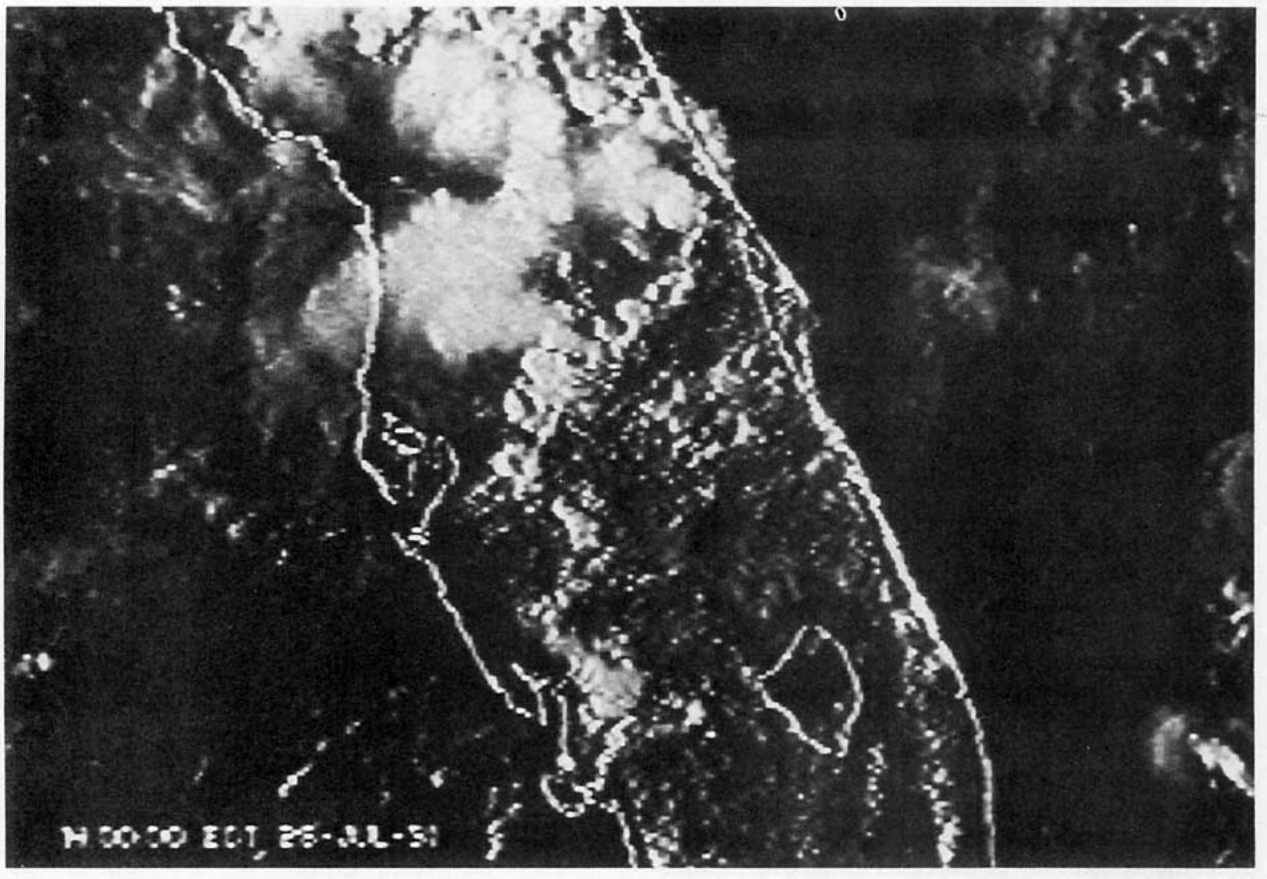

FIG. 2. Visible satellite image of central Florida at 1800 UTC 26 July 1991.

used to examine the radar measurements at the original sampling resolution using both sector and range–height indicator (RHI) scans. Computer-animated movies of reflectivity, horizontal winds, and convergence from data taken over approximately a 2.5-h period (40 volume scans) were created to better visualize the evolution of sea-breeze frontal circulations (including the trailing convergence line), thunderstorm outflows, and convection.

Both smoothed and nonsmoothed synthesized wind fields were examined within the Cartesian analysis grid. The smoothed horizontal wind field was obtained by first thresholding the interpolated radial velocity field with the signal-to-noise ratio and then applying a linear least squares two-dimensional filter to the radial velocity and synthesized horizontal wind fields. Convergence values were obtained from standard three-point centered differentiation.

The depth of sea breeze was generally between 300 and 400 m, except in local regions. The interpolated wind fields at the 600-m level provided important information about the wind field just above the sea breeze air and in local regions where the sea breeze penetrated this level. The 600-m synthesized winds interpolated from the two lowest elevations scans (0.3° and 1.0°) did not resolve the sea breeze well, and lower altitude syntheses did not have sufficient area-wide coverage. To obtain information about the low-level circulations over Merritt Island and Cape Canaveral, velocity fields were synthesized utilizing only the 0.3° elevation scans from each of the radars. We restricted this synthesis of two constant elevation surfaces to locations near the perpendicular bisector of the radar baseline where the heights of the center of the radar beams were within 50 m. This method allowed us to document flow features below 300 m.

Ground and tower measurements also provided important information about circulations within the boundary layer. Forty-seven PAM II stations, located throughout the CaPE study region, provided 1-min averages of temperature, humidity, pressure, and wind speed and direction. The Air Force/KSC tower network, concentrated on Merritt Island and Cape Canaveral, provided 5-min averages of temperature, and wind speed and direction at differing heights from 9 to 152 m. These data were examined and used in determining the surface position of the sea-breeze front and trailing convergence line.

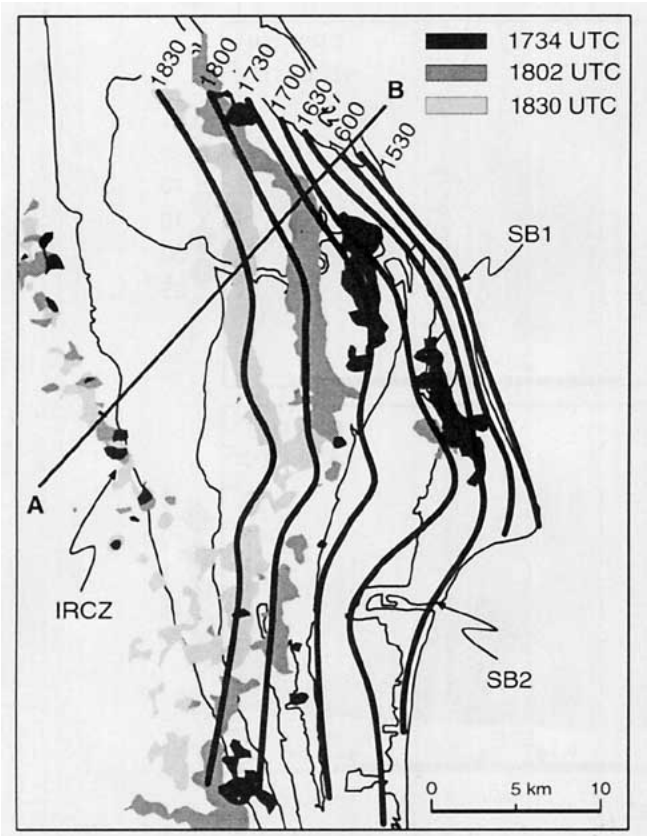

FIG. 3. Half-hourly (UTC) positions of the sea-breeze front derived from surface, tower, and radar reflectivity measurements. The CP-4 radar reflectivity (15-dBZ$_e$ contour) is also presented to show the sea-breeze front and Indian River convergence zone (IRCZ) at 1734, 1802, and 1830 UTC. The RHI on Fig. 5 is located along line *AB*.

3. Evolution of the sea-breeze front, river-breeze convergence zones, and the trailing convergence line

The background flow over central Florida west of Cape Canaveral, averaged over the lowest 1600 m from local soundings, was from the south-southwest at approximately 4 m s^{-1}. The southwesterly synoptic flow was associated with a weak upper-level trough that extended from Alabama to northern Florida on 26 July 1991. Figure 2 shows the cloud cover over central Florida at 1800 UTC (local time, EDT, is UTC − 4 h). Deep convection formed along a sea-breeze front near the west coast of Florida, which quickly moved inland under the influence of the prevailing winds. Over north-central Florida a line of intense thunderstorms, that formed early on 26 July, continued to develop southward and produce strong outflow boundaries. These outflow boundaries eventually moved through the CaPE study region, disrupting the sea-breeze flow.

The large-scale wind direction and wind speed on 26 July were similar to those that Zhong and Takle (1993) found to be ideal for the development of strong sea- and river-breezes in the Cape Canaveral area. In this section we will discuss these circulations as well as a trailing convergence line that developed within the sea breeze air.

a. Sea breeze and sea-breeze front

The sea-breeze front was the strongest boundary layer feature evident in the Cape Canaveral region during the early afternoon. Surface data over the region indicated that the local sea breeze tended to be perpendicular to the orientation of the nearest shore. This resulted in a sea-breeze front that was roughly the same shape as the coastline. Figure 3 shows the inland movement of the sea-breeze front for each half hour between 1530 and 1830 UTC, as revealed by PAM II, tower, and radar reflectivity data. The position of the sea-breeze front was clearly evident from a band of radar reflectivity (15-dBZ$_e$ filled contour) observed within each radar volume. Three examples of the reflectivity patterns are shown in Fig. 3 at 1734, 1802, and 1830 UTC. Because of the pronounced bend in the sea-breeze front evident on Fig 3, it is convenient to consider the sea-breeze front as composed of two sections, termed SB1 and SB2. The section of the sea-breeze front north of Cape Canaveral (SB1) was first observed at approximately 1530 UTC. It moved inland with a propagation speed of about 1–2 m s^{-1} and from an approximate direction of 75°, roughly perpendicular to the coastline. The surface flow behind SB1 was easterly at 5 m s^{-1}. The southern section of the sea-breeze front (SB2) developed near 1600 UTC. It propagated at 1–2 m s^{-1} from the southeast (~120°). The surface flow behind SB2 was south-southeasterly at approximately 5 m s^{-1}.

Surface station data showed distinct changes in both wind and temperature fields following the passage of the sea-breeze front. For example, Fig. 4 shows changes in surface conditions during the passage of the sea-breeze front at PAM Station 19 (see Fig. 1 for lo-

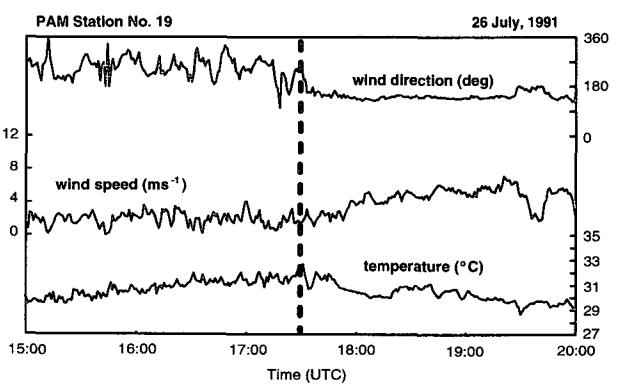

FIG. 4. Surface atmospheric conditions during the passage of the sea-breeze front. The 1730 UTC frontal passage at PAM station 19 (see Fig. 1 for location) is represented by the dotted line.

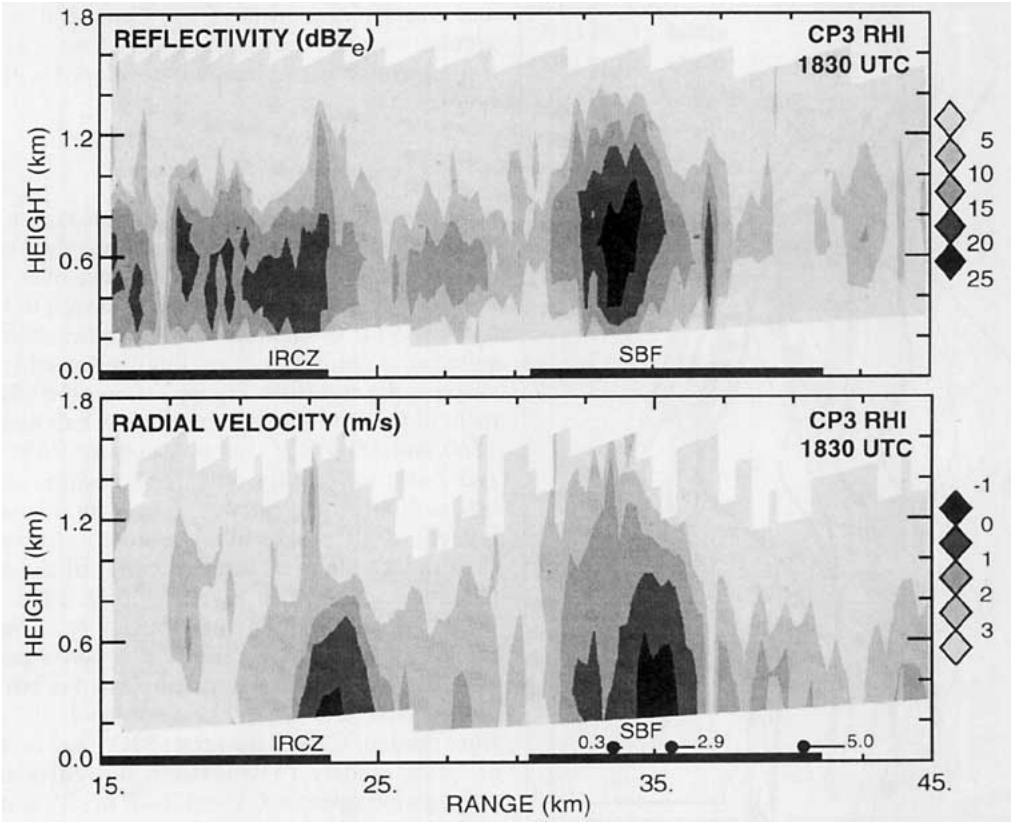

FIG. 5. RHI reflectivity and radial velocity from CP-3 through the sea-breeze front (SBF) and the Indian River convergence zone (IRCZ) at 1830 UTC. The RHI is along line *AB* shown in Fig. 3. The reflectivity field is contoured at 5-dBZ$_e$ intervals between 5 and 25 dBZ$_e$. The area of radar coverage for all reflectivities below 5 dBZ$_e$ is shown using the lightest gray shade. Radial velocity field is contoured at 1 m s^{-1} intervals between -1 (toward CP-3) and 3 (away from CP-3). Regions of radar coverage for all velocities above 3 m s^{-1} are shown using the lightest gray shade. The surface wind component along the cross section (m s^{-1}) are shown for three locations along the CP-3 radial over Merritt Island. Locations of land are represented by the heavy black lines at the bottom of the figure.

cation). The reduced variance in all quantities following the passage of the sea-breeze front points to the more convective nature of the air landward of the front. This is consistent with the usual case of convection being suppressed behind the sea-breeze front.

Figure 5 shows an RHI cross section of reflectivity and radial velocity at 1830 UTC from CP-3 through the sea-breeze front (SBF) and the Indian River convergence zone (IRCZ, discussed in section 3b) along line *AB* on Fig. 3. The sea-breeze front appears in both fields at a range of about 35 km. The inflow associated with the head of the sea-breeze front extended to approximately 600 m. The inflow behind the head of the sea-breeze front was sufficiently shallow that the radar was unable to observe it in the cross section. Therefore, wind data from three surface stations are plotted to show the presence of the inflow. Radial convergence is evident ahead of the leading edge of the sea breeze. This convergence was associated with the band of clouds evident from the reflectivity fields on Figs. 3 and 5. The cloud band formed within air that was lifted ahead of the sea-breeze front. The approximate cloud-top height, based on the 10-dBZ$_e$ contour, was 1.2 km.

The 1735 and 1935 UTC soundings taken during the Wyoming King Air takeoff and landing (shown in Fig. 6) provide information about the thermodynamic profile ahead of and behind the sea-breeze front. Figure 7 shows the aircraft track during the period in which these soundings were taken. During ascent, Melbourne Airport was to the west (inland) of the sea-breeze front. The aircraft then traveled northward, roughly parallel to the Indian River and west of the sea-breeze frontal positions at 1730 and 1800 UTC (see Fig. 3). During descent, the aircraft was generally above the sea breeze from 1935 to 1953 UTC. For a short period of time around 1944 UTC the aircraft descended into the top of the sea breeze at a height of about 410 m after which it climbed into the ambient air. After 1953 UTC the aircraft descended below 400 m into the sea breeze, remaining within the sea breeze until landing. Unre-

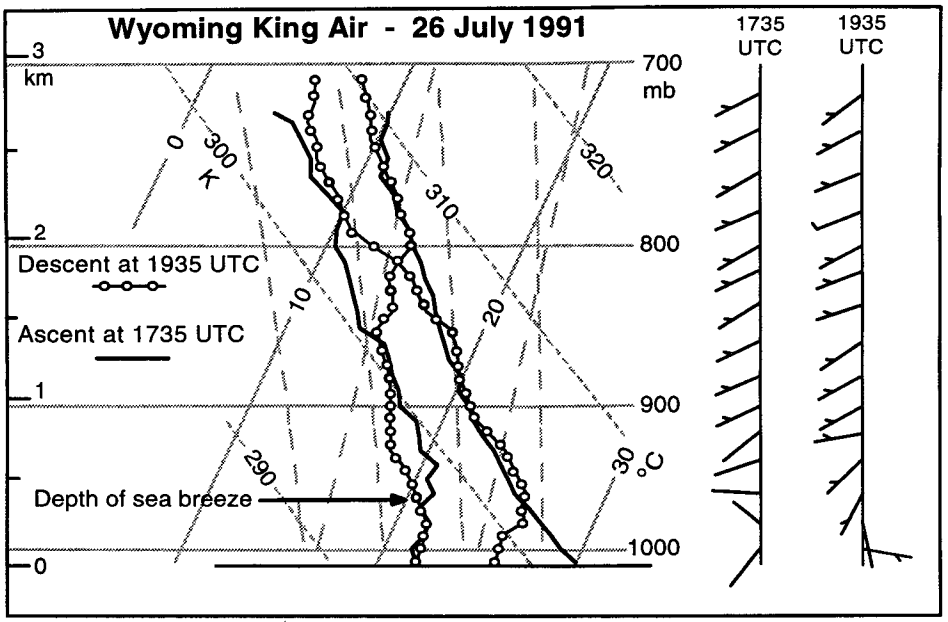

FIG. 6. Aircraft soundings taken by the Wyoming King Air during takeoff and landing at approximately 1735 and 1935 UTC, respectively. Wind barbs use standard convention.

presentative data collected during penetrations of an outflow boundary were excluded from the sounding taken during the aircraft descent. The excluded region is shown by the section of gray flight track in Fig. 7.

Data taken during the aircraft soundings illustrate changes in low-level atmospheric conditions with the passage of the sea-breeze front. At 1735 UTC the atmosphere was conditionally unstable from the surface to a height of at least 2.5 km. The winds throughout the layer had a westerly component. By 1935 UTC, after the sea-breeze front had penetrated far inland, the temperature had cooled at all levels below about 400 m, where the winds had developed an easterly component. Above 400 m the thermodynamic profile was similar to the 1735 UTC sounding.

b. Indian River convergence zone

The strongest convergence zone associated with the inland rivers formed during the early afternoon along the western shore of the Indian River. This convergence zone formed along the upwind (western) shore between the divergent flow associated with subsidence over the cool water (Indian River) and the southwesterly flow over the inland region of the Florida peninsula. A band of high reflectivity (>10 dBZ_e) associated with this convergence zone was located along the western shore of the Indian River (Fig. 3). Radar echoes associated with the Indian River convergence zone were first observed in the radar reflectivity field at 1700 UTC and remained essentially stationary for more than 2 h. Convergence on the downwind (eastern) shore was not well resolved by our data and would be expected to be much weaker. Convergence was evident along the western shore of the Indian River for nearly 40 km, with embedded regions of higher convergence at the 300-m level reaching values near 3×10^{-3} s^{-1}. The influence of the Indian River convergence zone is evident in Fig. 5 where air can be seen converging below 400 m near the shoreline. The cloud band in the reflectivity field in Fig. 3 is positioned over the region of maximum convergence inland of the western shoreline of the Indian River. The depth of the clouds that formed over the Indian River convergence zone was typically less than 1.0 km, slightly less than the clouds over the sea-breeze front.

As the southern section of the sea-breeze front (SB2) propagated inland, it collided with the southern portion of the Indian River convergence zone. Convection was initiated near the region where these two boundaries interacted. Several thunderstorm cells developed at these locations and moved eastward with the ambient flow. The convective cells that initiated at these interacting boundary layer features will be discussed in section 4.

c. Banana River convergence zone

A weaker convergence zone formed during the early afternoon along the upwind (western) shore of the Banana River, while an area of weak divergence was evident over the river. These features remained nearly stationary until the sea-breeze front passed at approximately 1730 UTC. As the sea-breeze front overtook

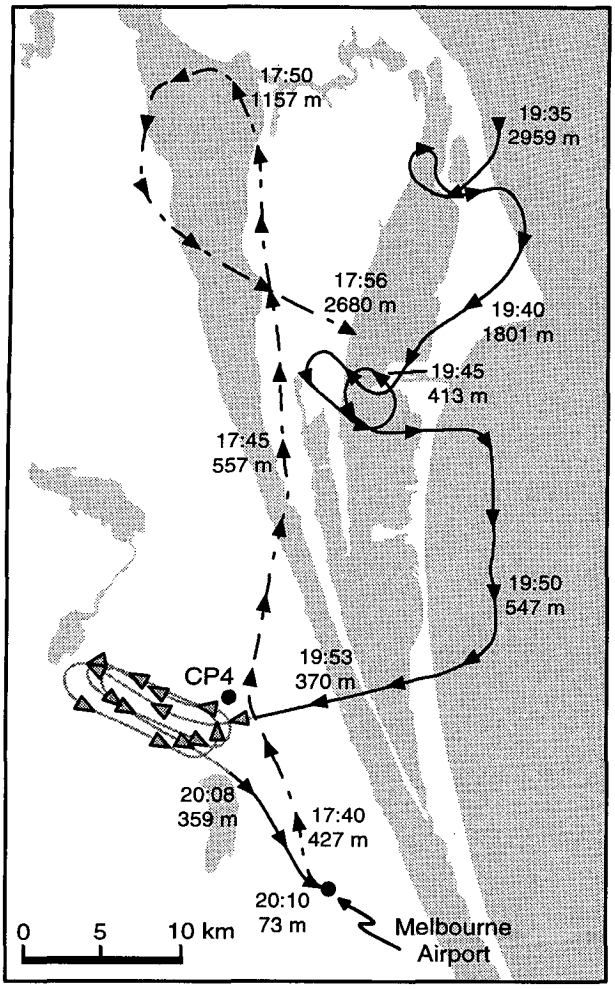

FIG. 7. Wyoming King Air flight track for takeoff and landing soundings (Fig. 6). Dashed line represents the takeoff track with aircraft height shown approximately every 5 min. Solid line represents the landing track, with gray track excluded from sounding.

the Banana River convergence zone there was a noticeable increase in the reflectivity along SB2. Both the divergent flow over the river and the convergence zone along its western shore remained evident for a short period of time following the sea-breeze frontal passage. Continued divergent flow over the Banana River after the sea-breeze front passed influenced the initial position of the trailing convergence line, as discussed in the following section.

d. Trailing convergence line

A persistent convergence line developed within the sea-breeze air as the two sections of the sea-breeze front, SB1 and SB2, moved inland. Figure 8 shows the wind field at 1830 UTC based on surface station data (Fig. 8a) and synthesized radar winds below 400 m (Fig. 8b) from the lowest elevation scans of CP-3 and

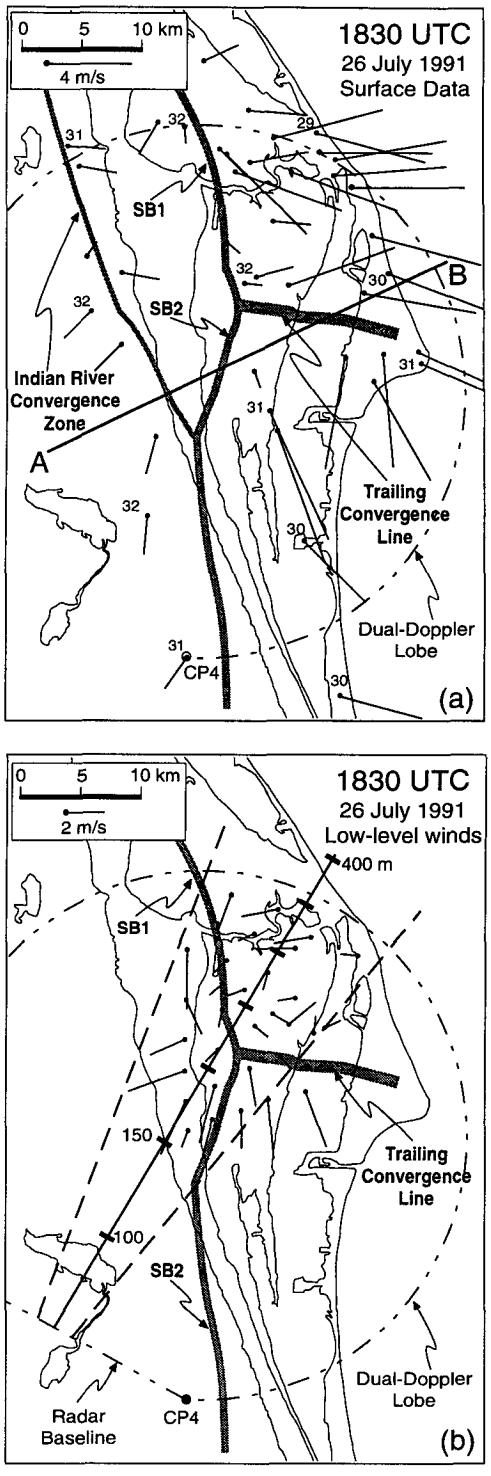

FIG. 8. Wind data at 1830 UTC showing the position of the Indian River convergence zone, SB1, SB2, and the trailing convergence line. The wind speed at each location is represented by the length of the wind barb. (a) Surface wind data. (b) Synthesized radar winds from lowest elevation scans of CP-3 and CP-4. The solid thin line represents the location where the heights of the center of the radar beams are equal. Heights are indicated every 50 m. The dashed thin lines indicate locations where the centers of the radar beams were separated by 40 m.

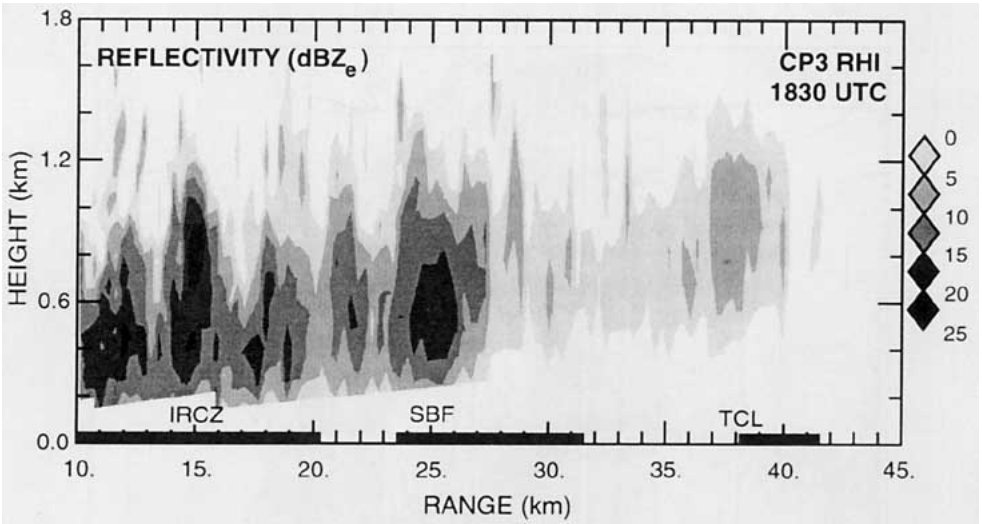

FIG. 9. Radar reflectivity RHI from CP-3 at 1830 UTC along line *AB* on Fig. 8a. The position of the trailing convergence line (TCL), the sea-breeze front (SBF), and the Indian River convergence zone (IRCZ) are shown. Reflectivity field is contoured at 5-dBZ_e intervals between 0 and 25 dBZ_e. Locations of land are represented by the heavy black lines at the bottom of the figure.

CP-4. Convergence in the surface winds is clearly visible extending from the intersection of SB1 and SB2 eastward toward the outer coast of Cape Canaveral. Radar synthesized winds show low-level southerly flow south of the trailing convergence line extending up to 200 m. The southwesterly and westerly winds north of the trailing convergence line at altitudes greater than 300 m are above the sea breeze, while winds between 250 and 300 m are near the top of the sea-breeze air. Winds west of the sea-breeze front between 150 and 300 m were generally southerly to southwesterly. Surface data showed that the trailing convergence line persisted from the time the sea breeze moved onshore at 1630 UTC to approximately 1935 UTC when a strong outflow boundary moved through the region from the north disrupting the sea breeze flow. Surface temperature data indicated virtually no temperature difference across the trailing convergence line.

The structure of the trailing convergence line is evident from both radar data and a sounding taken in its vicinity at 1730 UTC. Figure 9 shows an RHI scan taken through a portion of the trailing convergence line at 1830 UTC along line *AB* on Fig. 8a. The features with the highest reflectivities on the figure are 1.0-km-deep clouds associated with the sea-breeze front located at a range of 25 km and the Indian River convergence zone at a range of about 15 km. Behind the sea-breeze front few clouds were observed by radar. However, at a range of 38 km, stronger radar echoes can be seen between the 600- and 1200-m heights. These echoes are associated with a band of clouds that developed over the trailing convergence line above the sea breeze.

Figure 10a shows the location where a rawinsonde, launched from CCAS, passed through these clouds over the trailing convergence line at 1730 UTC. The thermodynamic profile from that sounding is shown in Figure 11. The rawinsonde first entered the cloud near 1.0 km and exited at 1.5 km. The low-level wind profile from the CCAS sounding was difficult to interpret since the rawinsonde rose through the trailing convergence line and encountered winds unrepresentative of the low-level profile behind either SB1 or SB2. The low-level winds in the region of the trailing convergence line are best illustrated in the surface and low-level synthesized data shown in Fig. 8a and Fig. 8b.

Figures 10a and 10b show the cloud band was nearly always present over the trailing convergence line near the intersection of SB1 and SB2, but the distance the band extended toward the Cape Canaveral coast decreased with time. We will show shortly, using dual-Doppler analyses, that the depth of the sea-breeze air along the trailing convergence line was greater than in other areas. Therefore, air above the sea breeze would be forced to ascend over the deeper sea-breeze air in the vicinity of the trailing convergence line. Before 1800 UTC, the trailing convergence line was oriented nearly perpendicular to the southwesterly synoptic wind. During this period, weak divergent flow over the Banana River was suggested by the limited PAM data available along the river shoreline. The shape of the reflectivity pattern along the trailing convergence line during this period corresponded approximately to the northeastern shoreline of the Banana River (Fig. 10a). This correspondence suggests that outflow off the Banana River initially influenced the position of the trail-

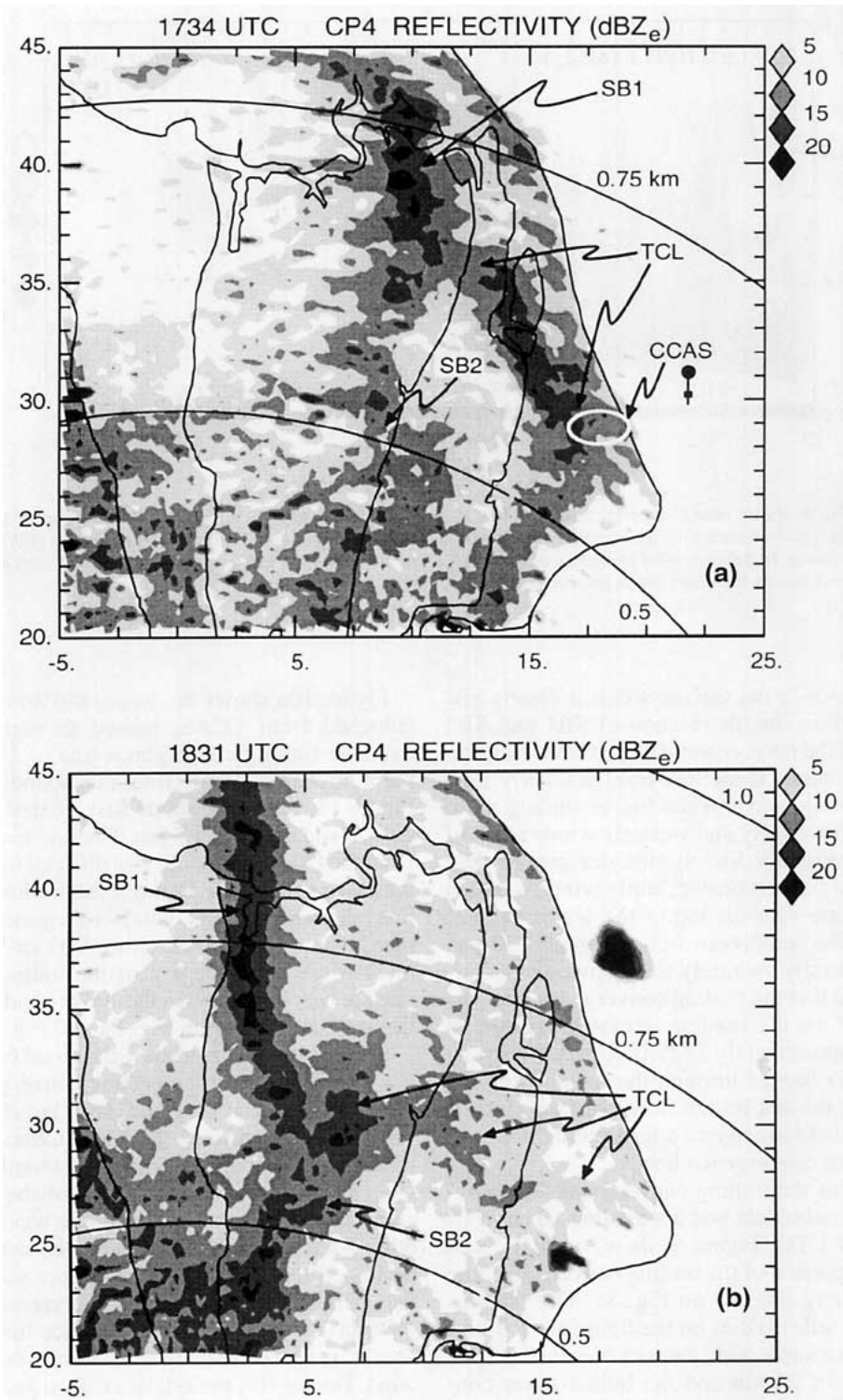

FIG. 10. (a) Reflectivity field from CP-4 at 1734 UTC showing positions of SB1, SB2, and the trailing convergence line (TCL). Reflectivity field is contoured at 5-dBZ$_e$ intervals from 5 to greater than 20 dBZ$_e$. Rings of constant height of the center of the radar beam are shown every 0.25 km. (b) Reflectivity field from CP-4 at 1831 UTC showing positions of SB1, SB2, and the trailing convergence line.

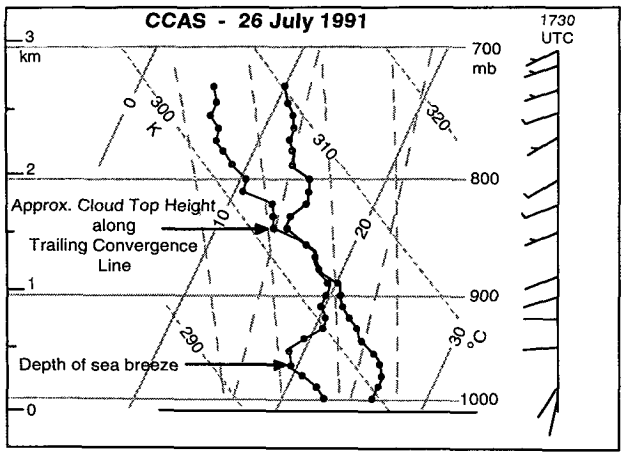

FIG. 11. Sounding from CCAS taken at 1730 UTC. Region where sounding penetrated the trailing convergence line clouds is shown in Fig. 10a.

ing convergence line. Later, as the trailing convergence line became more parallel to the ambient wind direction, the length of the cloud band decreased. As the sea-breeze front moved farther onshore the position of the trailing convergence line became less distinct in the radar reflectivity field as the cloud band dissipated over Cape Canaveral and the Banana River. However, the clouds at the inland end of the trailing convergence line continued to form as the ambient air was lifted over the sea breeze near the intersection of SB1 and SB2.

Synthesized wind fields at 600 m were developed for every volume between 1730 and 1940 UTC. Figure 12 shows an example of a 600-m dual-Doppler synthesized wind field at 1824 UTC. The 600-m wind field over Merritt Island and Cape Canaveral, consisting primarily of air originating west of the sea-breeze front, was typically southwesterly. As air approached the coast, the wind direction veered, so as to become perpendicular to the outer coastline. The veering in wind

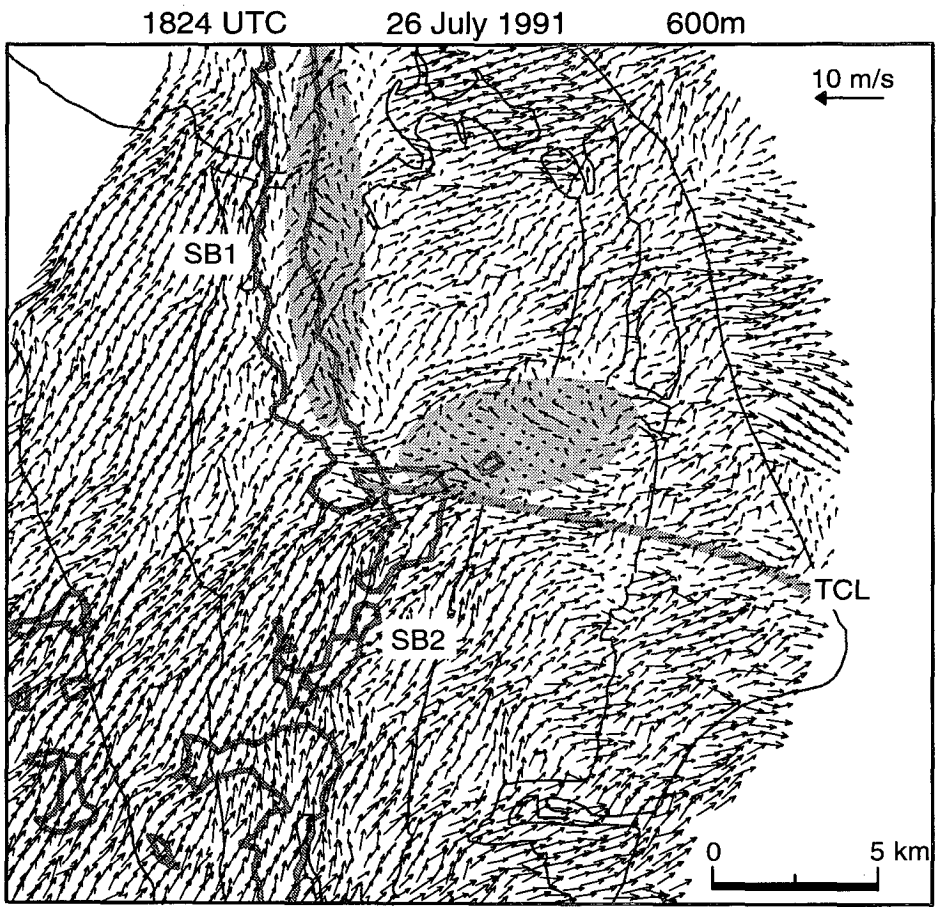

FIG. 12. Dual-Doppler synthesized wind field at 600 m at 1824 UTC. The 15-dBZ$_e$ reflectivity contour (dark gray line) indicates the position of SB1 and SB2. The surface position of the trailing convergence line is shown by a light gray line extending from the sea-breeze front eastward over Cape Canaveral. Two regions of easterly winds (sea-breeze air) along the head of the sea-breeze front and trailing convergence line are highlighted by gray-shaded areas.

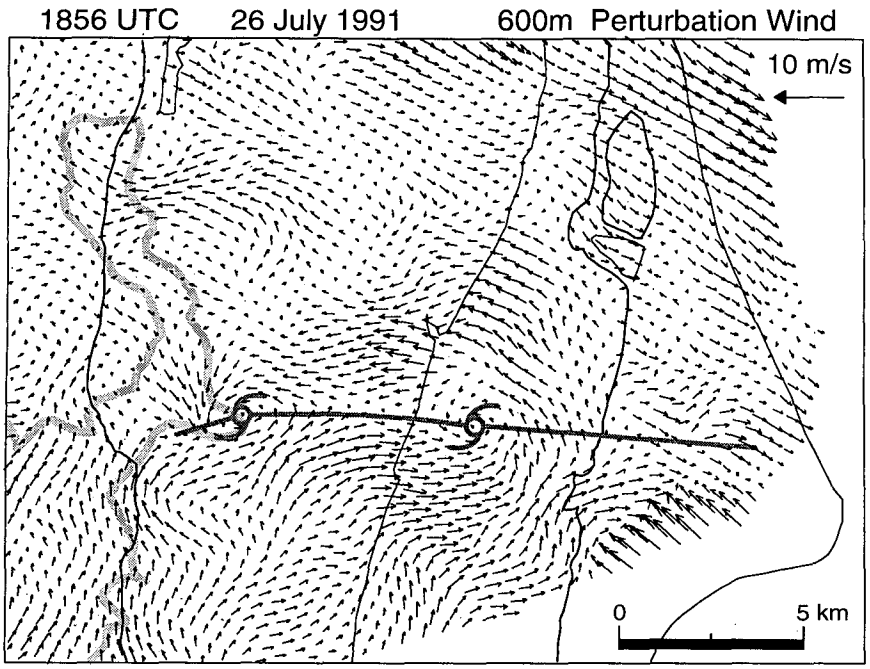

FIG. 13. Dual-Doppler perturbation wind field at 600 m at 1824 UTC with the mean wind of $U = 1.5$ m s^{-1}, $V = 0.5$ m s^{-1} subtracted. The sea-breeze front is shown by the 15-dBZ_e reflectivity contour (light gray line). The surface position of the trailing convergence line is indicated by the dark gray line. The locations of two vortices within the 600-m winds are shown along the trailing convergence line.

direction over this region is consistent with the weak off-shore pressure gradient expected with the sea breeze circulation at this height.

Sea-breeze air penetrated through the 600-m level near the trailing convergence line and at the head of the sea-breeze front north of the trailing convergence line. The sea breeze was deeper at the head of the sea-breeze front (northernmost gray-shaded region in Fig. 12 along SB1); however, easterly winds appeared only at the head of the sea-breeze front in syntheses after 1820 UTC. A distinct wind shift can be seen in Fig. 12 directly to the east of the intersection of SB1 and SB2 (southernmost gray-shaded region). This local region of easterly, onshore, winds developed just north of the surface position of the trailing convergence line, as determined from surface data. Unfortunately, we were unable to resolve vertical motions near the trailing convergence line (it was impossible to estimate an accurate lower boundary condition at the altitude of the lowest elevation scan, 250 m AGL); however, low-level convergence in this region must have induced vertical motions that resulted in a deepening of the easterly winds, making it possible for easterlies to appear within the 600-m interpolated wind field. The region of easterlies at 600 m near the trailing convergence line first appeared after the sea-breeze front passed over the Banana River (1810 UTC) and became more prominent with time until about 1935 UTC when the strong southward moving outflow boundary disrupted the sea breeze flow. The region of easterly winds along the trailing convergence line was at least 300 m deeper than the depth of the sea breeze (300–400 m) at other locations. It was evident from animations of the 600-m

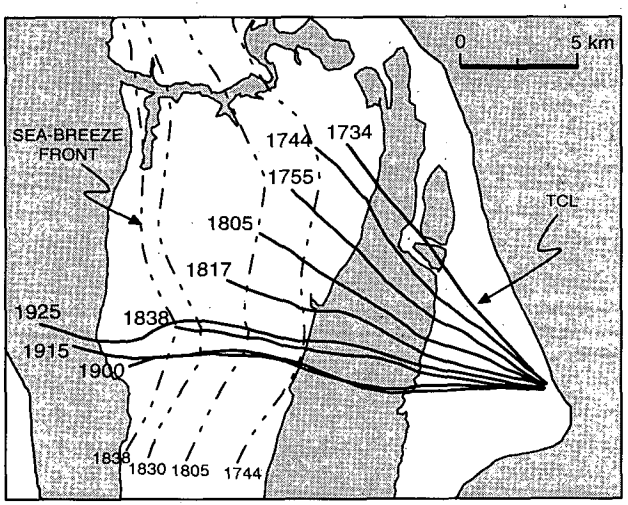

FIG. 14. Orientation and position of the trailing convergence line (solid line) determined from dual-Doppler radar observations and surface data for the period of 1734 to 1925 UTC. Dashed lines show the sea-breeze frontal position at several times.

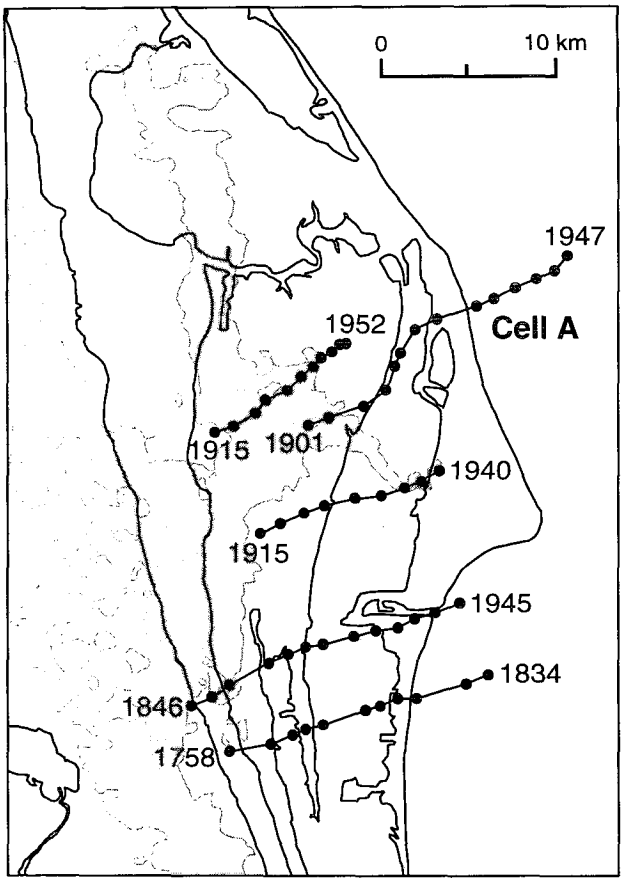

FIG. 15. Tracks of several thunderstorms including cell A. Positions are shown for each cell from first echo until dissipation, merger with other thunderstorms, or until left area of radar coverage. Filled contour of 10-dBZ$_e$ reflectivity shows locations of sea-breeze front and Indian River convergence zone at 1838 UTC.

dual-Doppler synthesized wind field that the region of deeper easterlies associated with the trailing convergence line provided an obstacle to the southwesterly ambient flow aloft. As the ambient southwesterly flow approached the region of deeper easterlies, the air aloft was forced around the sea-breeze air. This is most evident on Fig. 12, where narrow streams of accelerated air can be seen flowing around the sea-breeze air near the trailing convergence line.

This acceleration and change in direction of the ambient wind aloft resulted in the formation of two cyclonically rotating vortices. Figure 13 shows the perturbation wind field (mean wind subtracted) at 1856 UTC with two vortices clearly located along the southern boundary between the ambient air aloft and the elevated region of sea-breeze air. Both vortices developed at approximately 1830 UTC, as the sea-breeze front moved across Merritt Island, and were observed for nearly an hour (1830–1920 UTC). One vortex developed over the eastern shore of the Banana River and then traveled westward along the trailing convergence line until reaching the western shore of the river, where it remained nearly stationary. Another vortex formed over eastern Merritt Island and propagated directly behind the intersection of SB1 and SB2. Maximum values of the vertical component of vorticity observed within the vortices at 600 m were roughly 4×10^{-3} s^{-1}. We show in the next section that a thunderstorm formed in a region of strong convergence just north of the westernmost vortex.

A summary of the positions of the trailing convergence line based on Doppler radar observations (horizontal wind, convergence, and reflectivity fields) and surface station data from 1734 to 1925 UTC is shown in Fig. 14. The divergent flow that remained over the Banana River after the passage of the sea-breeze front initially increased the wind speed to the south of the trailing convergence line. This caused the trailing convergence line to be located closer to the shoreline north of Cape Canaveral. Later, as the sea breeze strengthened (see wind speed in Fig. 4), the influence of the weak divergent flow over the Banana River became less important, allowing the trailing convergence line to reposition. At 1810 UTC the deeper region of easterlies along the trailing convergence line first became apparent in the 600-m level wind field. Thereafter, the trailing convergence line remained nearly stationary and lengthened as the sea-breeze front moved inland until about 1930 UTC when a strong outflow boundary displaced the sea breeze.

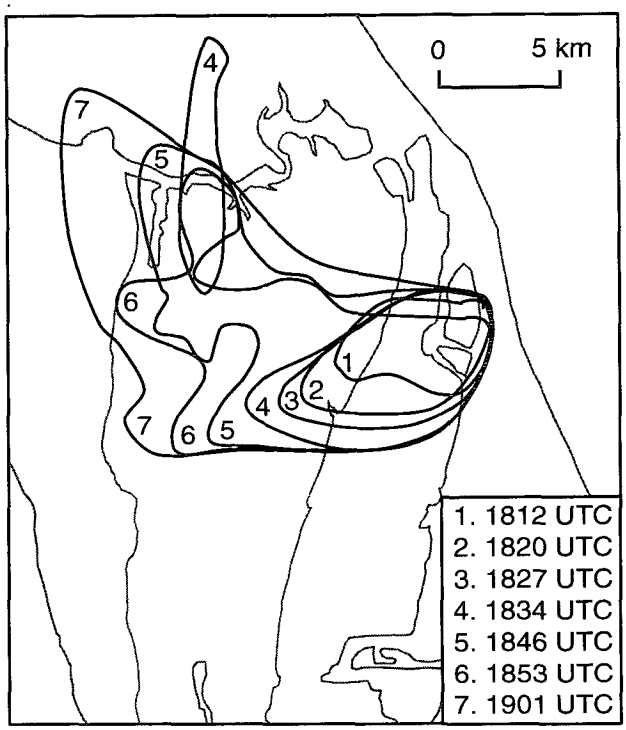

FIG. 16. Regions where sea-breeze easterlies were observed in the 600-m horizontal wind field at indicated times.

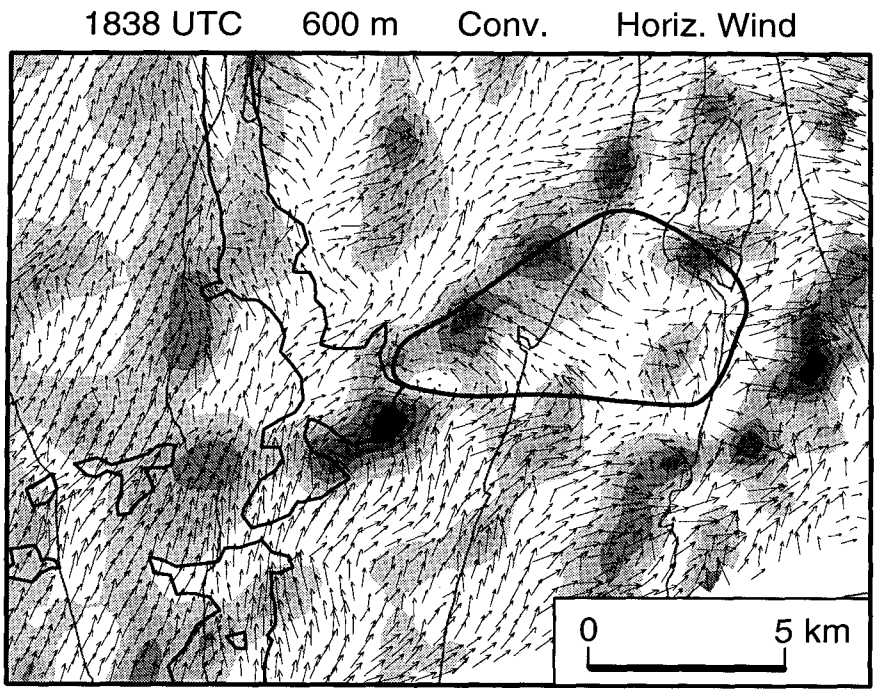

FIG. 17. Convergence at 600 m at 1838 UTC. Convergence is contoured at 0.5×10^{-3} s^{-1} intervals from 0.0 to 2.5×10^{-3} s^{-1}. Region outlined by thick black line shows area of easterly winds at the 600-m level. The sea-breeze front is shown by the 15-dBZ_e reflectivity contour (thin black line).

4. Formation and development of convection

Convection on 26 July over Merritt Island initiated at locations of enhanced low-level convergence at intersections of the boundary layer features discussed in section 3: the two branches of the sea-breeze front (SB1 and SB2), the trailing convergence line, the Indian River convergence zone, and thunderstorm outflow boundaries. First, a series of thunderstorms initiated along the western shore of the Indian River as the intersection point of the Indian River convergence zone and SB2 moved northward. During this period, a single intense convective cell also developed over central Merritt Island along the trailing convergence line near the juncture of SB1 and SB2. Finally, convection initiated over northern Merritt Island at two locations where the strong thunderstorm outflow boundary intersected the Indian River convergence zone and SB1. Each of these boundary layer interactions are discussed in this section.

a. Convection at intersection of sea-breeze front and Indian River convergence zone

A series of thunderstorms developed throughout the early afternoon (1700–1915 UTC) along the western shore of the Indian River at the intersection of SB2 and the Indian River convergence zone (Fig. 15). The Indian River convergence zone was nearly stationary while SB2 propagated inland with a speed of 1–2 m s^{-1} and an orientation of approximately 20° to the Indian River convergence zone. As a result, the point of intersection between the Indian River convergence zone and SB2 moved northward during the afternoon, and each new storm formed to the north of previous storms. Each thunderstorm moved northeastward over Merritt Island with the ambient flow above the sea breeze, and then dissipated over the ocean. Nearly all the cells developed precipitation cores with reflectivity values greater than 50 dBZ_e and many produced weak outflow boundaries east of the sea-breeze front.

b. Convection above the sea breeze and trailing convergence line

A strong convective cell (designated cell A) developed above the sea breeze along the trailing convergence line near its intersection with SB1 and SB2. To understand the origin of this cell one must first understand the topography of the top of the sea-breeze air. The top of the sea breeze air in most locations was located at about 400 m and deepened slowly with time. However, at the trailing convergence line, low-level convergence between the two sea-breeze flow regimes led to a local deepening of the sea-breeze air. Dual-Doppler syntheses at several levels in this region showed a local area of easterly momentum that "bulged" upward to above 600 m north of the surface

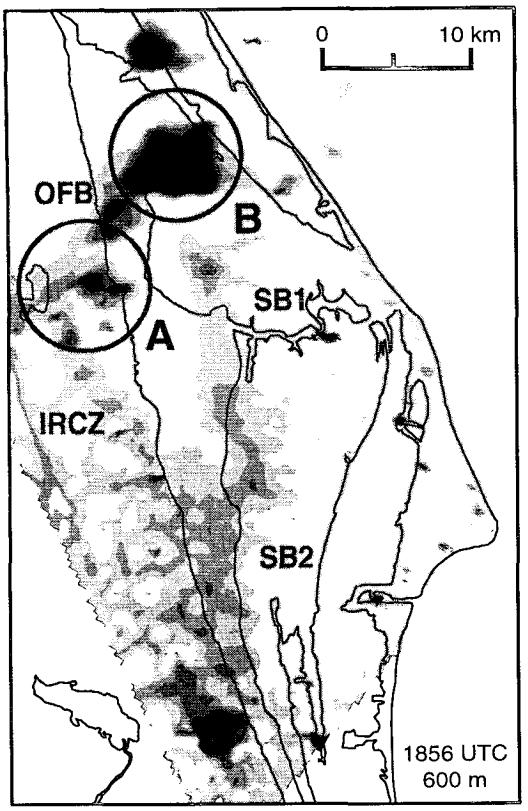

FIG. 18. Horizontal reflectivity fields from CP-4 at 600 m (shading represents values from 0 to greater than 50 dBZ_e at intervals of 10 dBZ_e) showing locations where thunderstorms developed as a strong outflow boundary (OFB) from northern storms intersected the Indian River convergence zone (circle A) and SB1 (circle B).

position of the trailing convergence line. This altitude was the approximate height of cloud base. The time evolution of the bulge of easterly winds is shown in Fig. 16. The deepening of the sea breeze in this local region began at approximately 1830 UTC, after the trailing convergence line had repositioned with an east–west orientation, and continued westward to merge with a bulge of easterly winds associated with the head of SB1.

Initially the bulge associated with the trailing convergence line appeared only at 600 m in a small area north of the trailing convergence line. As it grew, the bulge of easterly winds, evident in the outlined region in Fig. 17, led to the development of a local region of enhanced convergence near cloud base (~600 m) as the ambient southwesterly flow above the sea breeze collided with the bulging sea-breeze air just east of the intersection of SB1 and SB2. Based on the echo tracking in Fig. 15, the area of strong local convergence on Fig. 17 corresponded in time and space to the extrapolated position of cell A 23 min before the first detectable echo. Dual-Doppler wind and convergence fields showed that as the depth of the sea-breeze bulge increased in this local region, convergence was enhanced along its western boundary with a convergence maxima ($\sim 2.5 \times 10^{-3}$ s^{-1}) at the southwesternmost edge of the deeper easterlies. This region of locally enhanced convergence along the leading western edge of the deeper sea-breeze air was observed throughout several radar volumes at 300 and 600 m for a time period encompassing the estimated initiation time of cell A (~1845 UTC). The enhanced convergence region near the top of the sea breeze was just north of one of the two cyclonically rotating vortices. In fact, both the strong local convergence that gave rise to cell A and the vortices are manifestations of the forced acceleration of ambient southwesterly air around and over the developing bulge of sea-breeze air along the trailing convergence line. Cell A developed near the time that the strongest convergence occurred at 600 m. The enhanced convergence region eventually weakened at 600 m as the sea breeze continued to deepen. However, shortly after cell A formed, the sea breeze was completely disrupted by the strong southward-moving thunderstorm outflow boundary.

c. *Convection along a thunderstorm outflow boundary*

An outflow boundary from strong thunderstorms that formed earlier well north of Cape Canaveral (Fig. 2) progressed southward at approximately 8.0 m s^{-1}, reaching the northern tip of Merritt Island at about 1856 UTC (Fig. 18). Deep convection developed at the intersection of this strong outflow boundary and the Indian River convergence zone (circle A) and SB1 (circle B). Subsequent convection rapidly developed along the entire leading edge of the outflow boundary. These new convective storms produced additional outflow boundaries that passed over Merritt Island and Cape Canaveral at approximately 1930 UTC, disrupting the sea breeze.

5. Summary and conclusions

This study examined complex flow patterns associated with the Cape Canaveral sea breeze and sea-breeze front using dual-Doppler radar, sounding, and surface data collected during the Convection and Precipitation/Electrification (CaPE) Experiment. This case focused on (a) the structure of the sea breeze, an associated trailing convergence line, river-induced convergence zones, and thunderstorm outflow boundaries; (b) and the development of convection where these features interacted. Our observational study is the first to document the development and evolution of the trailing convergence line over Cape Canaveral and show that its presence can play a role in storm initiation. Our most important findings are the following:

1) Variations in the direction of the sea breeze in the vicinity of irregular coastlines, such as Cape Ca-

naveral, can lead to persistent zones of convergence within the sea-breeze air. These zones of convergence, in turn, can locally increase the depth of the sea-breeze air and create circulations at the top of the sea breeze that can support the development of convection.

2) Small inland water bodies, such as the Indian River, can have a strong influence on the location where thunderstorms first develop as the sea breeze propagates inland. Divergence over the small, relatively cooler Indian River during daytime was shown to be sufficient to maintain a quasi-stationary convergence zone which, when approached and disrupted by the sea-breeze front, triggered thunderstorms. The intersection point between the sea-breeze front and the river-induced convergence zone identified the location where successive thunderstorms developed during the day. Tracking this intersection point may be a predictor of future thunderstorm activity.

Observational and numerical studies should be conducted to determine the frequency, evolution, and characteristics of trailing convergence lines in this area and other regions with similarly complex coastlines. In general, the relative importance of coastline shape and inland water bodies on local convergence patterns, the structure of the sea breeze, and the initiation of convection under differing atmospheric conditions should be examined.

Acknowledgments. We would like to thank Bob Rilling (NCAR/RDP) and Steve Williams (NCAR/OFPS) for their valuable assistance in obtaining the radar, surface, tower, and sounding data that were taken during CaPE. Thanks are extended to Bill Andersen (NCAR/MMM) for his helpfulness with SPRINT and CEDRIC. The authors would also like to acknowledge several useful discussions during the CaPE scientific workshop, Boulder, Colorado (25–26 October 1993). This research was supported by the National Science Foundation under Grant NSF ATM 91-21698.

REFERENCES

Abbs, D. J., 1983: Sea-breeze interactions along a concave coastline in southern Australia: Observations and numerical modeling study. *J. Atmos. Sci.*, **40,** 1999–2009.

Arritt, R. W., 1989: Numerical modeling of the offshore extent of sea breezes. *Quart. J. Roy. Meteor. Soc.*, **115,** 547–570.

Atchison, M. K., and G. E. Taylor, 1992: Analyzing and forecasting sea breeze conditions at the Kennedy Space Center. Preprints, *Symp. on Weather Forecasting,* Atlanta, GA, Amer. Meteor. Soc., 132–138.

Byers, H. R., and H. R. Rodebush, 1948: Causes of thunderstorms of the Florida peninsula. *J. Meteor.*, **5,** 275–280.

Cautenet, S., and R. Rosset, 1989: Numerical simulation of sea breezes with vertical wind shear during dry season at Cape of Three Points, West Africa. *Mon. Wea. Rev.*, **117,** 329–339.

Frank, N. L., P. L. Moore, and G. E. Fisher, 1967: Summer shower distribution over the Florida peninsula as deduced from digitized radar data. *J. Appl. Meteor.*, **6,** 309–316.

Gentry, R. C., and P. L. Moore, 1954: Relation of local and general wind interaction near the sea coast to time and location of air-mass showers. *J. Meteor.*, **11,** 507–511.

Gray, B. M., 1991: CaPE experiment proceeds in Florida. *Bull. Amer. Meteor. Soc.*, **72,** 1287.

Lyons, W. A., R. L. Walko, M. E. Nicholls, R. A. Pielke, W. R. Cotton, and C. S. Keen, 1992: Observational and numerical modeling investigations of Florida thunderstorms generated by multi-scale surface thermal forcing. Preprints, *Fifth Conf. on Mesoscale Processes,* Atlanta, GA, Amer. Meteor. Soc., 85–90.

McPherson, R. D., 1970: A numerical study of the effect of a coastal irregularity on the sea breeze. *J. Appl. Meteor.*, **9,** 767–777.

Miller, L. J., C. G. Mohr, and A. J. Weinheimer, 1986: The simple rectification of Cartesian space of folded radial velocities from Doppler radar sampling. *J. Atmos. Oceanic Technol.*, **3,** 162–174.

Mohr, C. G., and R. L. Vaughan, 1979: An economical procedure for Cartesian interpolation and display of reflectivity data in three-dimensional space. *J. Appl. Meteor.*, **18,** 661–670.

——, L. J. Miller, and R. L. Vaughan, and H. W. Frank, 1986: The merger of mesoscale datasets into a common Cartesian format for efficient and systematic analyses. *J. Atmos. Oceanic Technol.*, **3,** 144–161.

National Research Council, 1992: *Coastal Meteorology: A Review of the State of the Science.* National Academy Press, 99 pp.

Nicholls, M. E., R. A. Pielke, and W. R. Cotton, 1991: A two-dimensional numerical investigation of the interaction between sea breezes and deep convection over the Florida peninsula. *Mon. Wea. Rev.*, **119,** 298–323.

Pielke, R. A., 1974: A three-dimensional numerical model of the sea breezes over south Florida. *Mon. Wea. Rev.*, **102,** 115–139.

——, 1984: *Mesoscale Meteorological Modeling.* Academic Press, 612 pp.

Taylor, G. E., M. K. Atchison, and C. R. Parks, 1990: The Kennedy Space Center Atmospheric Boundary Layer Experiment (KABLE) Phase II, Final Report. National Aeronautics and Space Administration (NASA), Kennedy Space Center (KSC), 226 pp. [Available from ENSCO, Inc., 445 Pineda Court, Melbourne, FL 32940.]

Wakimoto, R. M., and N. T. Atkins, 1994: Observations of the sea-breeze front during CaPE. Part I: Single-Doppler, satellite and cloud photogrammetry analysis. *Mon. Wea. Rev.*, **122,** 1092–1114.

Watson, A. L., R. L. Holle, R. E. Lopez, R. Ortiz, and J. R. Nicholson, 1991: Surface wind convergence as a short-term predictor of cloud-to-ground lightning at Kennedy Space Center. *Wea. Forecasting,* **6,** 49–64.

Zhong, S., and E. S. Takle, 1993: The effects of large-scale winds on the sea–land-breeze circulations in an area of complex coastal heating. *J. Appl. Meteor.*, **32,** 1181–1195.

——, J. M. Leone Jr., and E. S. Takle, 1991: Interaction of the sea breeze with a river breeze in an area of complex coastal heating. *Bound.-Layer Meteor.*, **56,** 101–139.